Successive destruction of charge density wave states by pressure in LaAgSb$_2$

Kazuto Akiba [ORCID],[*] Hiroaki Nishimori, Nobuaki Umeshita, and Tatsuo C. Kobayashi

Graduate School of Natural Science and Technology, Okayama University, Okayama 700-8530, Japan

We comprehensively studied the magnetotransport properties of LaAgSb$_2$ under high pressure up to 4 GPa, which showed unique successive charge density wave (CDW) transitions at $T_{CDW1} \sim 210$ K and $T_{CDW2} \sim 190$ K at ambient pressure. With the application of pressure, both T_{CDW1} and T_{CDW2} were suppressed and disappeared at the critical pressures of $P_{CDW1} = 3.0$–3.4 GPa and $P_{CDW2} = 1.5$–1.9 GPa, respectively. At P_{CDW1}, the Hall conductivity showed a steplike increase, which is consistently understood by the emergence of a two-dimensional hollow Fermi surface at P_{CDW1}. We also observed a significant negative magnetoresistance effect when the magnetic field and current were applied parallel to the c axis. The negative contribution was observed in the whole pressure region from 0 to 4 GPa. Shubnikov–de Haas (SdH) oscillation measurements under pressure directly showed the changes in the Fermi surface across the CDW phase boundaries. In $P < P_{CDW2}$, three major oscillation components, α, β, and γ, were identified, whose frequencies were increased by application of pressure. The increment rate of these frequencies was considerably larger than that expected from the shrinkage of lattice constant, indicating the unignorable band modification under pressure. In the normal metallic phase above $P > P_{CDW1}$, we observed a single frequency of ~ 48 T with a cyclotron effective mass of $0.066m_0$, whose cross section in the reciprocal space corresponded to only 0.22% of the first Brillouin zone. Besides, we observed another oscillation component with frequency of ~ 9.2 T, which is significantly enhanced in the limited pressure range of $P_{CDW2} < P < P_{CDW1}$. The amplitude of this oscillation was anomalously suppressed in the high-field and low-temperature region, which cannot be explained by the conventional Lifshitz-Kosevich formula.

I. INTRODUCTION

The charge density wave (CDW) has long been known as a macroscopic quantum state, which shows a static order of charge carrier accompanied by lattice modulation. Several three-dimensional materials with anisotropic crystal structure and Fermi surface show spontaneous formation of a CDW state with a lattice modulation wave number of $\boldsymbol{Q}$ by lowering the temperature [1]. Following the Peierls transition in a one-dimensional system, the mechanism of the CDW is frequently understood as a nesting of Fermi surfaces connected by a nesting vector $\boldsymbol{Q}$, which results in an opening of the energy gap at the the nested region. The vanishing of the corresponding Fermi surface considerably alters the density of state at the Fermi level and causes drastic changes in various physical properties. In real three-dimensional materials with multiple Fermi surfaces, however, it is a long-standing issue under intense discussion whether the formation of a CDW can be understood fully with only the Fermi surface properties [2,3].

The layered intermetallic compound LaAgSb$_2$, the target of the present study, forms a tetragonal crystal structure ($P4/nmm$, space group No. 129) [4], as shown in Fig. 1(a). Ag and Sb form a layered structure similar to the iron-based superconductors [5], in which Sb1 forms square nets and Ag is located in a slightly distorted tetrahedron formed by Sb2. La is located between these layers in an alternating manner along the c axis.

LaAgSb$_2$ has been known to exhibit successive CDW transitions at $T_{CDW1} \sim 210$ K and $T_{CDW2} \sim 190$ K. An x-ray diffraction study [6] revealed that CDW1 has a lattice modulation along the a axis characterized by modulation vector $(0.026 \times 2\pi/a, 0, 0)$, while CDW2 has a modulation along the c axis with modulation vector $(0, 0, 0.16 \times 2\pi/c)$, where a and c represent the lattice constants. Both CDW1 and CDW2 have been explained as a result of Fermi surface nesting [6]. The phase transition to the CDW1 can be observed as a clear humplike anomaly in the temperature dependence of the resistivity [7]. Compared to CDW1, the phase transition to CDW2 causes a smaller anomaly in the electrical transport, which is barely observed in the out-of-plane resistivity [6,8]. This difference has been explained as a larger segment of the Fermi surface being gapped by the CDW1 transition, which causes a significant change in the carrier density.

The Fermi surfaces of LaAgSb$_2$ have been studied by quantum oscillation measurements [9–11] combined with first-principles calculations and angle-resolved photoemission spectroscopy (ARPES) measurements [12,13]. Although several controversial conclusions can be seen in previous literature (e.g., regarding the shape of Fermi surfaces and correspondence of Fermi surface cross sections with quantum-oscillation frequencies), LaAgSb$_2$ is considered to have four Fermi surfaces: two-hole Fermi surfaces around the Γ point, a two-dimensional hollow electron surface, and an ellipsoidal electron surface around the X point [9]. Intriguingly, a recent ARPES measurement reported that the hollow Fermi surface, which is considered responsible for the nesting of CDW1, hosts a Dirac-cone-like dispersion in the vicinity of the Fermi
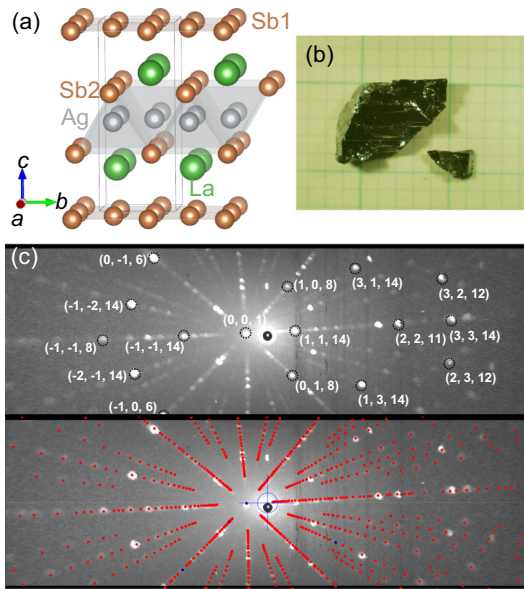
*akb@okayama-u.ac.jp

FIG. 1. (a) Crystal structure of LaAgSb$_2$. Shaded surfaces represent the square net formed by Sb1 and the tetrahedron formed by Sb2. (b) A picture of LaAgSb$_2$ single crystal utilized in the present study. The smallest square in the background is 1 mm×1 mm. (c) Back-reflection Laue pattern of LaAgSb$_2$ single crystal with x-ray beam parallel to the c axis. The lower panel shows the simulated pattern using crystallographic data obtained by single-crystal structural analysis.

TABLE I. Crystallographic data and refinement statistics for x-ray single-crystal structural analysis at ambient pressure and $T = 240$ K.

Formula	LaAgSb$_2$
crystal system	tetragonal
space group	$P4/nmm$ (No. 129)
a (Å)	4.3941(18)
c (Å)	10.868(6)
volume (Å^3)	209.84(17)
Z value	2
$R1$ [$I > 2\sigma(I)$]	0.0302

In the case of LaAuSb$_2$, both T_{CDW1} and T_{CDW2} are suppressed by application of pressure, and disappear at 1.7 GPa and 0.75 GPa, respectively [19].

The application of pressure and chemical substitution of La/Ag sites are known as effective methods to control T_{CDW1} and T_{CDW2} in LaAgSb$_2$ [20–22]. However, chemical substitution usually introduces lattice defects and unintentional carrier doping, which hinders systematic investigation of the CDW states. In contrast, high pressure is a useful external parameter that is free from the problems mentioned above. However, the effect of pressure on the electronic state has only been studied below 2.1 GPa [20,21], which is insufficient to eliminate the CDW1. At present, the critical pressures of the CDWs in LaAgSb$_2$ has remained unclear.

To clarify the complete pressure-temperature phase diagram of CDWs and to investigate the change in Fermi surfaces by application of pressure, we comprehensively studied magnetotransport properties of LaAgSb$_2$ under high pressure up to 4 GPa.

level [13]. Although a part of this linear dispersion is considered to be gapped by the formation of CDW1 at ambient pressure, the large linear magnetoresistance that is frequently observed in Dirac fermion systems and the existence of high-mobility carriers have been reported in a magnetotransport study [14]. If we can eliminate CDW1 by tuning an external parameter, we can expect the full contribution of the Dirac-like dispersion that is hidden by the CDW energy gap at ambient pressure. Thus, LaAgSb$_2$ can be a typical example to investigate the exotic transport phenomena originating from the Dirac fermion and the interplay between CDW formation and the presence of the Dirac fermion.

Replacement of the Ag site with its homologs, Au and Cu, has been known to cause a drastic change in the CDW properties. In LaCuSb$_2$, the temperature dependence of the resistivity is monotonic in contrast with LaAgSb$_2$ [15], and no phase transition has been reported to date. However, LaAuSb$_2$ shows a CDW transition with a clear humplike anomaly at $T_{CDW1} \sim 100$ K in resistivity [16,17], as well as LaAgSb$_2$, though the T_{CDW1} is considerably lower than that of LaAgSb$_2$. The dimensionality of the Fermi surfaces is considered a possible factor to determine the occurrence of CDW [18], though the specific origin of this difference is not clear at the present stage. Interestingly, in a recent study of LaAuSb$_2$, it has been reported that there exists a secondary CDW transition at $T_{CDW2} \sim 90$ K at ambient pressure [19], suggesting that LaAuSb$_2$ and LaAgSb$_2$ have quite similar CDW phase diagrams. Thus, it is important to compare and contrast the CDW properties between LaAgSb$_2$ and LaAuSb$_2$ to understand the origin of the CDW formation in this material class.

II. EXPERIMENTAL METHODS

Single crystals of LaAgSb$_2$ were obtained by the Sb self-flux method [7]. La (99.9%), Ag (99.99%), and Sb (99.9999%) with a molar ratio of 1:2:20 were placed in an alumina crucible, and sealed in a quartz ampoule with argon gas. After the mixture was heated to 1150 °C, it dwelled at this temperature for 12 hours. Then, it was cooled to 670 °C for 110–120 h. The flux was removed using a centrifuge separator. A picture of the as-grown single crystal is shown in Fig. 1(b). Most of the crystals obtained by the above method were millimeter-size lumps or plates. The crystals were appropriately shaped into rectangles for electrical resistivity measurements.

x-ray single-crystal structural analysis at ambient pressure and $T = 240$ K was performed using VariMax with Saturn (RIGAKU) with monochromated Mo K$_\alpha$ radiation ($\lambda = 0.71075$ Å). The obtained data collections are listed in Tables I and II. Laue diffraction measurement was performed using IPX-YGR (IPX Co., Ltd.) with back-reflection configuration. We obtained quite clear Laue spots, as shown in Fig. 1(c), which is explained by the identified crystallographic data and indicates the high quality of our single crystal.

The electrical transport under high pressure was measured by an indenter-type pressure cell ($P < 4$ GPa) [23]. Daphne oil 7474 [24] was used as a pressure medium. The pressure

TABLE II. Atomic coordinates (x, y, z) and equivalent isotropic atomic displacement parameters (U_{eq}) at ambient pressure and $T = 240$ K.

Atom	Site	x	y	z	U_{eq} (Å^2)
La	2c	1/4	1/4	0.23969(10)	0.0095(3)
Sb1	2a	3/4	1/4	0	0.0110(4)
Sb2	2c	3/4	3/4	0.33036(11)	0.0102(4)
Ag	2b	3/4	1/4	1/2	0.0133(4)

in the sample space was determined by the superconducting transition temperature of Pb set near the sample.

Temperature dependence of the resistivity at zero field was measured by using a gas-flow-type optical cryostat (Oxford Instruments, $T > 2$ K) and by a standard four-terminal method with a 2400 sourcemeter and 2182A nanovoltmeter (Keithley Instruments). The effect of thermal electromotive force by temperature gradient was removed by inversion of the current (I) direction.

The transverse magnetoresistivity ρ_{xx}, longitudinal magnetoresistivity ρ_{zz}, and Hall resistivity ρ_{yx} in magnetic fields were measured using a PPMS (Quantum Design, $B < 9$ T and $T > 2$ K), or superconducting magnet with a variable-temperature insert (Oxford Instruments, $B < 8$ T and $T > 1.6$ K). For the latter system, an LR-700 AC resistance bridge (Linear Research) was utilized with a measurement frequency of 16 Hz. Measurements were performed by the standard four-terminal method, and electrical contacts were formed by silver paste (Dupont 4922N).

III. RESULTS AND DISCUSSION

First, we focus on the temperature dependence of the in-plane resistivity (ρ_{ab}) at several pressures up to 3.8 GPa. At ambient pressure, we observed an abrupt increase in ρ_{ab} at 204 K, as indicated by a blue arrow in Fig. 2(a), which is ascribed to T_{CDW1}. This value agrees with the previous reports [6,7,20–22]. With the increment in pressure, T_{CDW1} monotonically decreased, and could not be defined above 3.4 GPa. Complementary, the temperature dependence of Hall resistivity ρ_{yx} at $B = 2$ T is shown in Fig. 2(b). At all pressures below 3.0 GPa, a clear increase in ρ_{yx} was observed at T_{CDW1}, which may correspond to the disappearance of partial Fermi surfaces due to the transition to CDW1. Above 3.4 GPa, however, ρ_{yx} did not show an increase and hardly depended on pressure. These results indicate that the critical pressure of CDW1 (P_{CDW1}) lies between 3.0 and 3.4 GPa. ρ_{yx} divided by the applied B is the Hall coefficient R_H, which is represented by $R_H = 1/[e(n_h - n_e)]$ in the high-field limit of the simple electron-hole conduction model with closed Fermi pockets. Here, n_h, n_e, and e represent the hole carrier density, electron carrier density, and elemental charge, respectively. However, because the Fermi surface of LaAgSb$_2$ has a complicated geometry, R_H cannot be connected simply with the carrier density, as discussed later. Thus, we do not enter the quantitative analysis of R_H in the present study.

As suggested by previous studies, an anomaly at T_{CDW2} is quite subtle in ρ_{ab}, and we could not trace the pressure dependence of T_{CDW2} in the in-plane transport. Thus, we focused on
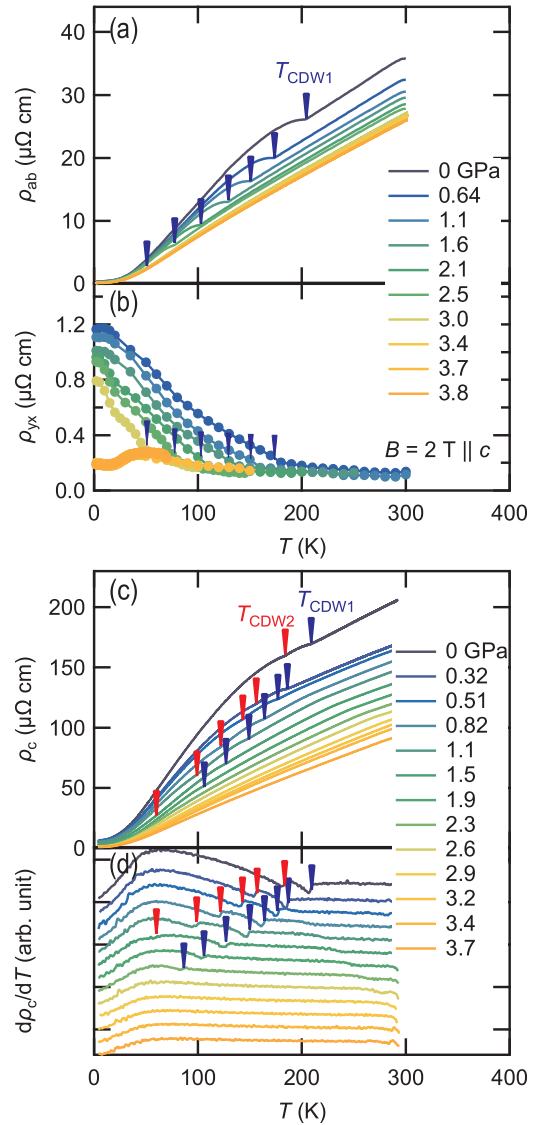

FIG. 2. (a) Temperature dependence of the in-plane resistivity (ρ_{ab}) at several pressures. Blue arrows indicate the transition temperature to CDW1 (T_{CDW1}). (b) Temperature dependence of Hall resistivity ρ_{yx} at $B = 2$ T at several pressures. (c) Temperature dependence of out-of-plane resistivity (ρ_c) at several pressures. Red arrows indicate the transition temperature to CDW2 (T_{CDW2}). (d) Temperature derivative of out-of-plane resistivity $d\rho_c/dT$ at several pressures. The traces are vertically shifted for clarity.

the out-of-plane resistivity (ρ_c) to identify T_{CDW2}. Figure 2(c) shows the temperature dependence of ρ_c at several pressures. $T_{CDW1} = 209$ K is also clearly observed in ρ_c, whose pressure dependence is consistent with that in Figs. 2(a) and 2(b). Furthermore, we can identify a kink at 184 K at ambient pressure, as indicated by a red arrow in Fig. 2(c). This is consistent with the transition temperature to CDW2 reported in the previous study [6,8], and thus, we hereafter define this anomaly as T_{CDW2}. As clearly observed in the $d\rho_c/dT$ in Fig. 2(d), T_{CDW2} was suppressed by pressure and became invisible above 1.9 GPa. From this result, we determined that the critical pressure of the CDW2 (P_{CDW2}) lies between 1.5 and 1.9 GPa.
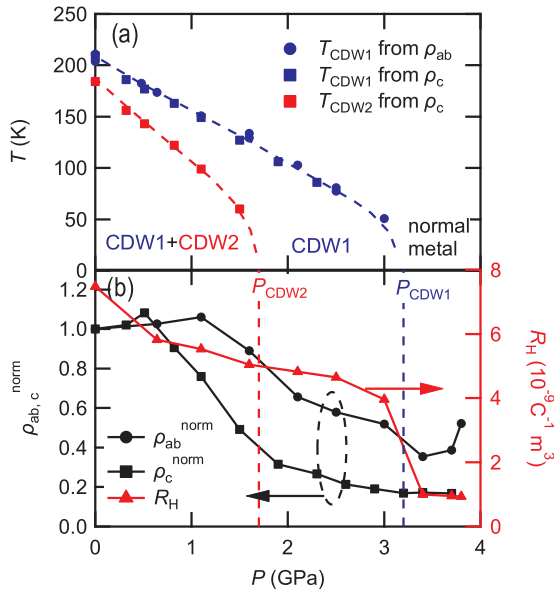
FIG. 3. (a) Pressure-temperature phase diagram of LaAgSb$_2$. The blue and red colors indicate T_{CDW1} and T_{CDW2}, respectively, and circular and rectangular markers indicate the transition temperature determined from ρ_{ab} and ρ_c, respectively. (b) Pressure dependencies of the in-plane resistivity at 2 K (ρ_{ab}^{norm}), out-of-plane resistivity at 3.7 K (ρ_c^{norm}), and Hall coefficient (R_H). ρ_{ab}^{norm} and ρ_c^{norm} were normalized by values at ambient pressure, and R_H was defined at $T = 2$ K and $B = 2$ T. Vertical broken lines indicate the critical pressures of CDWs determined in the present study.

We summarize the pressure dependence of T_{CDW1} and T_{CDW2} in Fig. 3(a). T_{CDW1} values determined from ρ_{ab} and ρ_c both lie on an identical line, and the slope is determined to be $dT_{CDW1}/dP \sim -51$ K/GPa. This value is slightly steeper than that reported in previous results (-43 K/GPa) [20,21], but shows reasonable agreement. Compared to T_{CDW1}, T_{CDW2} is more rapidly suppressed by pressure with slope of $dT_{CDW2}/dP \sim -80$ K/GPa. Both T_{CDW1} and T_{CDW2} depend linearly on the pressure sufficiently above P_{CDW1} and P_{CDW2}, whereas they seem to more rapidly approach zero in the vicinity of their critical pressure than in a simple linear extrapolation. We note that dT_{CDW1}/dP and dT_{CDW2}/dP in LaAuSb$_2$ are estimated to be -60 and -120 K/GPa, respectively [19], suggesting that CDW order in LaAgSb$_2$ is more robust against the application of pressure than that of LaAuSb$_2$. The black traces in Fig. 3(b) show the pressure dependencies of the in-plane resistivity at 2 K (ρ_{ab}^{norm}) and out-of-plane resistivity at 3.7 K (ρ_c^{norm}) normalized by values at ambient pressure. Up to P_{CDW1}, ρ_{ab}^{norm} shows decreasing trend. In the normal metallic phase above P_{CDW1}, on the other hand, ρ_{ab}^{norm} changes its slope and shows a rather weak pressure dependence. ρ_c^0 also changes its slope at P_{CDW2} and P_{CDW1}, and is almost constant in the normal phase. A similar change in the slope at P_{CDW1} is also reported in the pressure dependence of the in-plane residual resistivity of LaAuSb$_2$ [19]. The red trace in Fig. 3(b) shows R_H defined by ρ_{yx} at $B = 2$ T, which shows a significant decrease at P_{CDW1}.

To obtain more insight on the change in electronic structure across P_{CDW2} and P_{CDW1}, we investigated the in-plane magne-
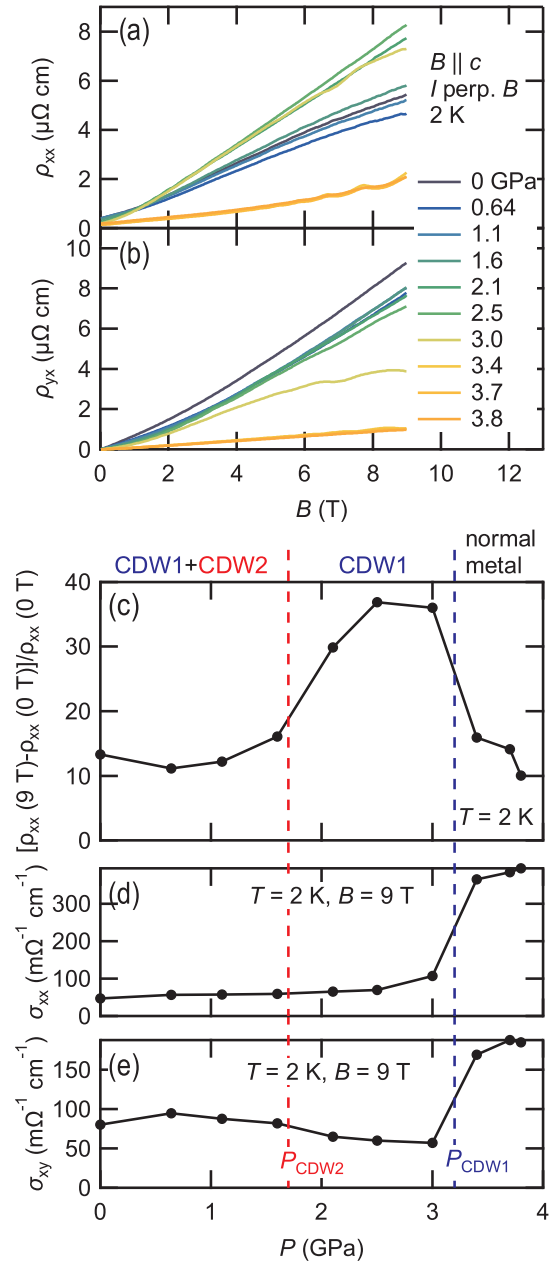

FIG. 4. (a) In-plane magnetoresistivity (ρ_{xx}) and (b) Hall resistivity (ρ_{yx}) at 2 K at several pressures. (c) Pressure dependence of magnetoresistivity at 2 K normalized by zero-field value [$\rho_{xx}(9 \text{ T}) - \rho_{xx}(0 \text{ T})]/\rho_{xx}(0 \text{ T})$. Pressure dependence of (d) σ_{xx} and (e) σ_{xy} at 2 K and 9 T.

toresistivity (ρ_{xx}) and Hall resistivity (ρ_{yx}) under high pressure with magnetic fields along the c axis and electric current within the a-b plane, whose results are shown in Figs. 4(a) and 4(b). ρ_{xx} at 2 K does not show the tendency of saturation and has quasilinear magnetic-field dependence rather than the conventional quadratic one at all measured pressures. ρ_{yx} at ambient pressure shows almost identical property with the previous report [14] and is significantly suppressed above 3.4 GPa. In addition, we can see nonmonotonic modulation superposed on ρ_{xx} and ρ_{yx}, which is notably enhanced above 3.4 GPa. This is ascribed to quantum oscillation, whose details
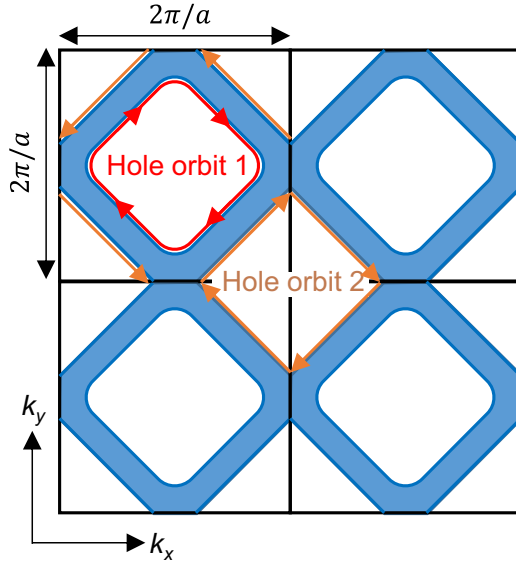
FIG. 5. Schematic picture of two-dimensional hollow Fermi surface of LaAgSb$_2$ in the k_x-k_y plane. The black square represents the first Brillouin zone of the tetragonal cell. The electron carrier occupies in the blue-shaded area. Possible closed orbits are indicated by red and orange loops.

will be discussed later. As shown in Fig. 4(c), the magnetoresistance effect shows characteristic behavior in each CDW phases. Below P_{CDW2}, in which CDW1 and CDW2 coexist, the magnetoresistance effect at 9 T is approximately 10–20 and shows weak pressure dependence. In the intermediate pressure range between P_{CDW2} and P_{CDW1}, in which only CDW1 survives, it is drastically enhanced up to 40. In the normal phase above P_{CDW1}, it rapidly decreases and again shows weak pressure dependence.

Using the data shown in Figs. 4(a) and 4(b), we deduced the pressure dependence of the in-plane electrical conductivity $\sigma_{xx} = \rho_{xx}/(\rho_{xx}^2 + \rho_{yx}^2)$ and Hall conductivity $\sigma_{xy} = \rho_{yx}/(\rho_{xx}^2 + \rho_{yx}^2)$ at $T = 2$ K and $B = 9$ T, as shown in Figs. 4(d) and 4(e). Both σ_{xx} and σ_{xy} show a steplike increase at P_{CDW1}, while there is no apparent change at P_{CDW2}. σ_{xx} in the normal metallic phase is approximately 8 times larger than that at ambient pressure, indicating the realization of a highly conductive phase above P_{CDW1}. σ_{xy} is represented by $\sigma_{xy} = (n_h - n_e)e/B$ in the case of a simple closed Fermi surface and $\omega_c \tau \gg 1$, where ω_c and τ represent the cyclotron frequency and relaxation time, respectively. However, it should be noted that this picture cannot be applied directly in a complicated Fermi surface, as in LaAgSb$_2$. More elementarily, σ_{xy} is represented by the following expression with the cross sections of hole-like orbit $S_h(k_z)$ and electron-like orbit $S_e(k_z)$ cut by a constant-k_z plane [25]:

$$\sigma_{xy} = \frac{e}{4\pi^3 B} \int dk_z [S_h(k_z) - S_e(k_z)]. \quad (1)$$

Here, the hole-like and electron-like orbits represent the trajectories that enclose the higher- and lower-energy regions in the momentum space, respectively. Let us consider a Fermi surface shown in Fig. 5, which is a simplified hollow Fermi surface of LaAgSb$_2$. As mentioned above, the CDW1 is re-
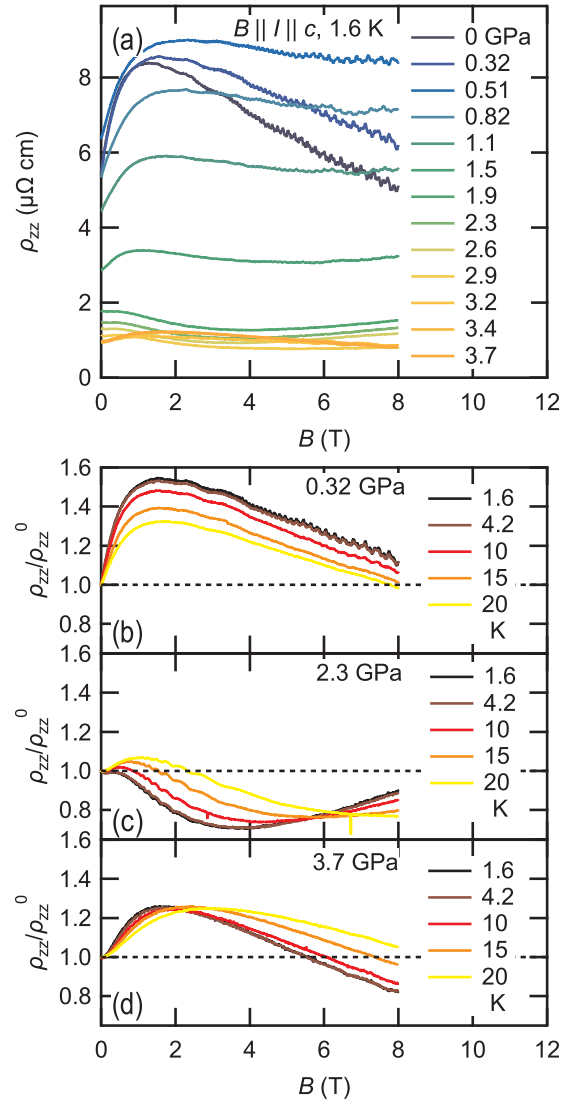

FIG. 6. (a) Out-of-plane magnetoresistivity (ρ_{zz}) at 1.6 K at several pressures. Temperature variation of out-of-plane magnetoresistivity normalized by zero-field value (ρ_{zz}/ρ_{zz}^0) at (b) 0.32, (c) 2.3, and (d) 3.7 GPa.

garded to result from a nesting within this Fermi surface. In the first Brillouin zone, this Fermi surface hosts two types of closed orbit indicated by red and orange loops. Because both orbits enclose a hollow region (high-energy region), these orbits should bring a positive contribution to σ_{xy}. This Fermi surface is more or less gapped out in the presence of CDW1; thus, the positive contribution to σ_{xy} should be suppressed below P_{CDW1}. Above P_{CDW1}, on the other hand, this Fermi surface fully contributes to the electrical transport, which results in enhancement of σ_{xy}. This scenario qualitatively agrees with the steplike increase in electrical conductivities at P_{CDW1}. The absence of an anomaly at P_{CDW2} may suggest that the formation of CDW2 brings modest effect in the in-plane orbital motion.

We also investigated the out-of-plane magnetoresistivity (ρ_{zz}) at 1.6 K and up to 3.7 GPa, which is shown in Fig. 6(a). At ambient pressure, ρ_{zz} rapidly increases as B increases

and has a local maximum at approximately 1 T. In higher B, we observed notable negative magnetoresistance effect, i.e., the decrease in ρ_{zz} as a function of B. Figure 6(b) shows the out-of-plane resistivity normalized by the zero-field value (ρ_{zz}/ρ_{zz}^0) at 0.32 GPa. The local maximum decreases as the temperature increases, whereas the slope of the negative magnetoresistance effect is less sensitive to the temperature. Compared to ρ_{xx}, very clear SdH oscillation superposed on the negative magnetoresistance was observed in the high-field region. With increments in pressure up to P_{CDW2}, the quasi-linear negative slope in the high-field region was gradually suppressed, as shown in Fig. 6(a), though local maximum still exists at ~1 T. After P passes through P_{CDW2}, the increase in ρ_{zz} below 1 T was hardly observed at 1.6 K, though it appeared as the temperature increases, as shown in Fig. 6(c). The origin of the drastic change in the functional form of ρ_{zz}/ρ_{zz}^0 is unclear at the present stage. In the normal metallic phase above P_{CDW1}, the increase in resistivity below 1 T and SdH oscillation were again observed at 1.6 K. As shown in Fig. 6(d), the negative slope of ρ_{zz}/ρ_{zz}^0 at 3.7 GPa is almost identical to that at 0.32 GPa.

In the conventional Drude model, ρ_{zz} remains unchanged as a function of magnetic field since the current parallel to the field direction is free from Lorentz force. An artificial negative longitudinal magnetoresistance effect is known to be caused by an extrinsic mechanism called current jetting [26,27], which becomes dominant in systems with large non-saturating ρ_{xx} and high mobility. In such a system with large anisotropy factor ρ_{xx}/ρ_{zz}, the electric current in the sample becomes strongly inhomogeneous in high magnetic fields, and artificial negative longitudinal magnetoresistance can appear depending on the geometry of the potential contact. As for the present case, let us assume that ρ_{zz} does not drastically change from the zero-field value, i.e., remains on the order of 1 $\mu\Omega$ cm. Then, ρ_{xx}/ρ_{zz} is estimated to be on the order of 1, since Fig. 4(a) indicates that ρ_{xx} is also on the order of 1 $\mu\Omega$ cm in the present magnetic field and pressure range. Thus, this extrinsic mechanism is excluded from the possible origin. We regard that the observed negative longitudinal magnetoresistance arises from the intrinsic electronic structure. The negative longitudinal magnetoresistance effect is often discussed in Dirac/Weyl systems, which is called the chiral anomaly [28,29]. In this mechanism, charge carriers are pumped from one Weyl point to another with opposite chiralities via the lowest Landau level in the presence of B parallel to the electric field. However, we observed negative contribution in all pressure from ambient pressure to 4 GPa, and no apparent enhancement was observed above P_{CDW1}, which is evident in comparison between Figs. 6(b) and 6(d). This result suggests that the presence of the two-dimensional hollow Fermi surface, in which possible Dirac dispersion has been proposed, causes little influence on the emergence of a negative contribution. On the other hand, recent theoretical study showed that a negative magnetoresistance effect can arise from the warp of the Fermi surface from the perfect sphere, regardless of the nontrivial band topology [30]. Thus, more details of the Fermi surfaces in both CDW phase and normal metallic phase under high pressure are indispensable to discuss the origin of negative longitudinal magnetoresistance. Here, we also note that isostructural LaAu$_x$Sb$_2$, which

shows CDW transitions at ~97 K at ambient pressure, shows weak positive longitudinal magnetoresistance at ambient pressure up to 8 T (Fig. 13 in the Appendix). The sample size and configurations of electrical contact are almost identical with those in LaAgSb$_2$. This supports that the remarkable negative longitudinal magnetoresistance is unique to the electronic structure of LaAgSb$_2$.

Then, we focus on the oscillatory structure on ρ_{xx}. Figure 7(a) shows the magnetic-field derivative of ρ_{xx} at 2 K as a function of B^{-1}. At ambient pressure, the oscillation is discernible above 4 T, and the oscillation pattern changes with application of pressure up to 3.8 GPa. In particular, we can recognize a drastic change in oscillation pattern when P passes through P_{CDW1}. The oscillation above 4 T is periodic with respect to B^{-1} and damps as the temperature increases, which is well described by the conventional Lifshitz-Kosevich (LK) formula for quantum oscillation phenomena [31]. Thus, this can be ascribed to Shubnikov–de Haas (SdH) oscillation by the extremum cyclotron orbit of the Fermi surfaces. Below 4 T [dotted region in Fig. 7(a)], on the other hand, we can also recognize another oscillatory structure with lower frequency between P_{CDW2} and P_{CDW1}. This oscillation is also assumed to be SdH oscillation, though its amplitude shows anomalous temperature/magnetic-field dependence unlike those above 4 T. In the following, we first focus on the oscillation structure observed above 4 T, and the oscillation observed below 4 T will be discussed later.

Figures 7(b) and 7(c) show the fast Fourier transform (FFT) spectra of $d\rho_{xx}/dB$ at various pressures. The FFT was performed in the magnetic field region between 4 and 9 T. At ambient pressure, we identified six peaks, as indicated by arrows in Figs. 7(b) and 7(c). Following the previous quantum oscillation studies [9–11], the peaks with frequencies $F = 67$, 164, and 436 T are labeled as the α, β, and γ peaks, respectively. These peaks show quite well accordance with the previous studies as shown in Table III. The peak at 327 T is assigned to be the second harmonic of β since the pressure dependence of the frequency is identical with that of β. The adopted temperature and magnetic-field range are different from those in previous studies, and thus, an oscillatory component higher than 600 T was not identified in the present study. In the pressure region below P_{CDW2}, we recognized several FFT peaks below 60 T, though it was difficult to trace the reliable pressure dependence. As the pressure approaches P_{CDW2}, all these peaks got gradually weaker and we could not trace the pressure dependence above 2.5 GPa. Then, above P_{CDW1}, a single oscillation with frequency of 48 T becomes dominant. At 3.0 and 3.4 GPa, just above P_{CDW1}, secondary oscillation components with frequencies of 25 and 94 were also identified.

Then, we focus on the quantum oscillation in ρ_{zz}. Figure 8(a) shows the out-of-plane magnetoresistivity with fourth-polynomial background subtraction. Compared with the in-plane magnetotransport, oscillation structure is quite sharp in the field region above 4 T, and another oscillation component below 4 T also appeared in the pressure region $P_{CDW2} < P < P_{CDW1}$. Figure 8(b) shows the FFT spectra of SdH oscillation above 4 T. We identified β, 2β, and γ peaks at ambient pressure, whose frequencies agree quite well with those in in-plane magnetotransport. We also identified an
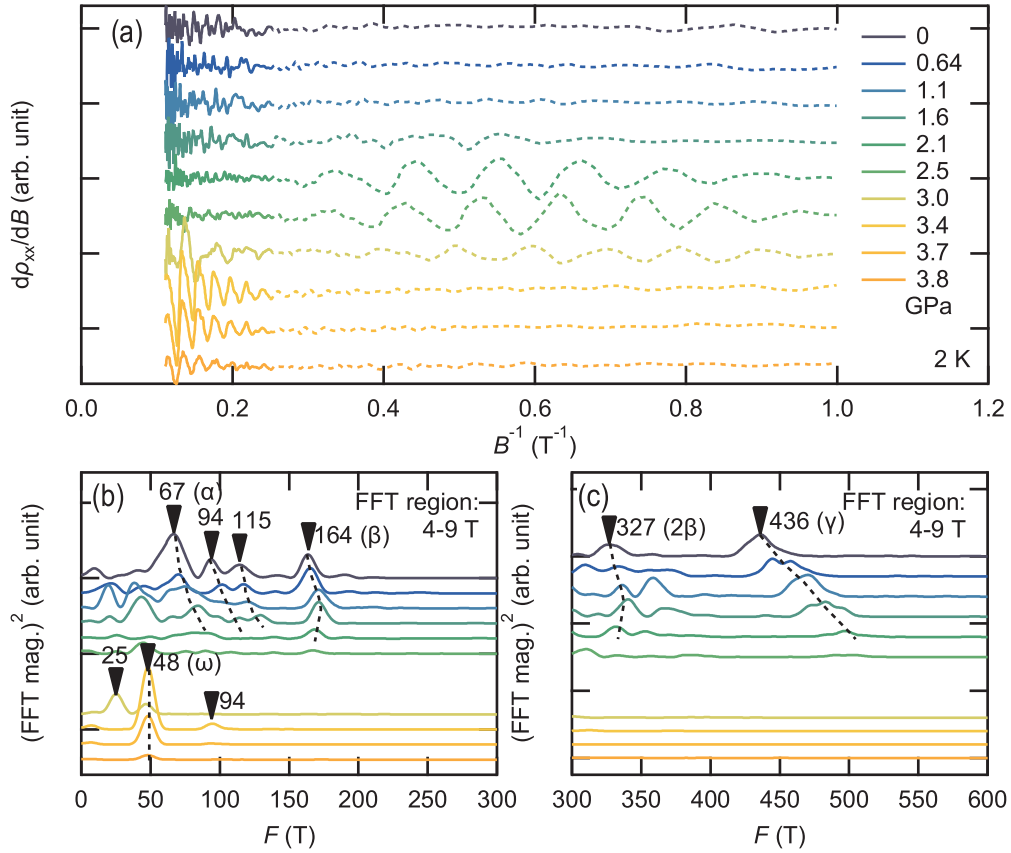
FIG. 7. (a) Magnetic-field derivative of in-plane magnetoresistivity ($d\rho_{xx}/dB$) at 2 K as a function of B^{-1}. The solid and broken region indicates the magnetic field of 4 T < B < 9 T and 1 T < B < 4 T, respectively. FFT spectra of $d\rho_{xx}/dB$ (b) up to $F = 300$ T and (c) above $F = 300$ T. In (b) and (c), the FFT was performed in 4 T < B < 9 T. Peaks are indicated by solid arrows with each frequency. FFT spectra at 3.0, 3.4, 3.7, 3.8 GPa are multiplied by 0.1 to make uniform the height of peaks.

oscillatory component with small frequency of ∼8 T [indicated by vertical broken lines and frequency scale in Fig. 8(a)], which has not been reported in previous studies. As seen in Fig. 8(b), the FFT peaks become gradually weak, and we could not see any discernible peak between P_{CDW2} and P_{CDW1}. Above P_{CDW1}, a single peak with $F = 47$ T appeared, which is also consistent with Fig. 7.

The pressure dependencies of the FFT peaks obtained from ρ_{xx} and ρ_{zz} measurements are summarized in Fig. 9(a). α, β, γ, and ω shift almost linearly with the increment in pressure, while only β showed tendency of saturation as it approaches

P_{CDW2} and slight decrement in $P_{CDW2} < P < P_{CDW1}$. In general, the cross section of a Fermi surface becomes larger as the first Brillouin zone is enlarged by shrinkage of the lattice constant. Using the linear compressibility of the in-plane lattice parameter $\frac{1}{a_0}\frac{da}{dP} = -2.9 \times 10^{-3}$ GPa^{-1} [20], the pressure derivative of the SdH frequency due to the shrinkage of the lattice constant is estimated as $\frac{1}{F_0}\frac{dF}{dP} = 5.8 \times 10^{-3}$ GPa^{-1}. Here, a_0 and F_0 represent the in-plane lattice constant and SdH frequency at ambient pressure. The pressure dependence of the lattice constant is approximated to be linear for simplicity.

TABLE III. The oscillation frequency (F), cyclotron effective mass (m_c), Dingle temperature (T_D), and pressure derivative normalized by ambient-pressure value ($\frac{1}{F_0}\frac{dF}{dP}$) obtained in the present study. F and m_c are obtained from ρ_{xx} data at ambient pressure unless otherwise specified by footnotes. Data in the parentheses are taken from the previous studies.

Label	F (T)	m_c (m_0)	T_D (K)	$\frac{1}{F_0}\frac{dF}{dP}$ (GPa^{-1})
α	67 (72 [9])	0.057 ± 0.001		0.16 ± 0.04
	94			0.135 ± 0.001
	115			0.07 ± 0.02
β	164 (164 [9], 160 [10])	0.154 ± 0.006 (0.16 [9], 0.16 [10])	(0.67 [10])	0.033 ± 0.005
γ	436 (432 [9], 440 [10])	0.26 ± 0.02[a] (0.28 [9], 0.34 [10])	(1.1 [10])	0.081 ± 0.004 (0.16 [9])
ω	48[b]	0.066 ± 0.001[b]	34 ± 2[b]	0.04 ± 0.01

[a]Data obtained from ρ_{zz} at 0.32 GPa.
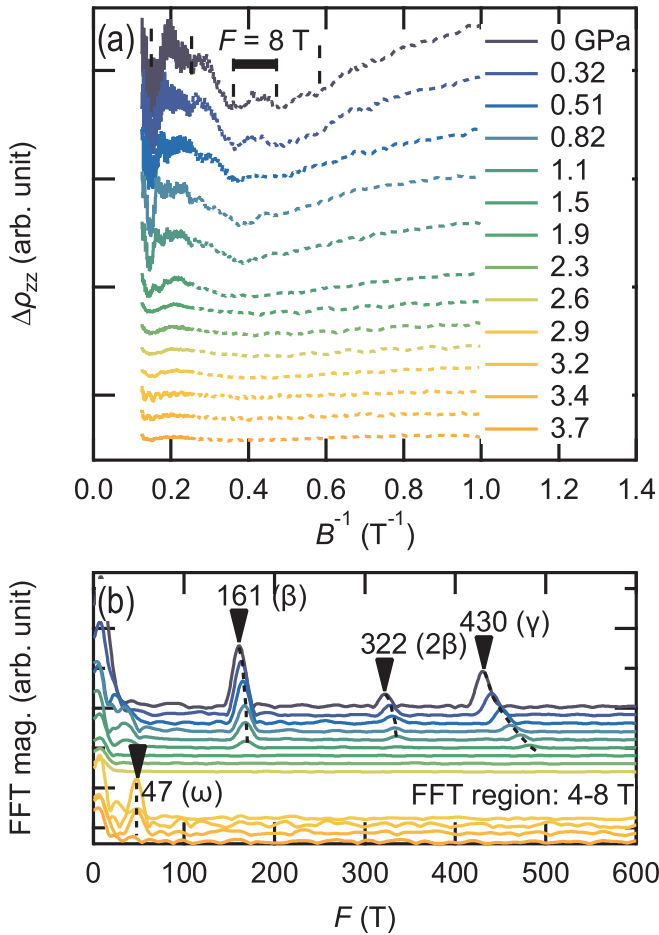[b]Data obtained from ρ_{xx} at 3.4 GPa.

FIG. 8. (a) Oscillatory component of the out-of-plane magnetoresistivity ($\Delta\rho_{zz}$) at 2 K as a function of B^{-1}. $\Delta\rho_{zz}$ was obtained by subtraction of fourth-polynomial background from ρ_{zz}. The solid and broken region indicates the magnetic field of $4\,\text{T} < B < 8\,\text{T}$ and $1\,\text{T} < B < 4\,\text{T}$, respectively. (b) FFT spectra of $\Delta\rho_{zz}$ obtained from magnetic-field region of $4\,\text{T} < B < 8\,\text{T}$. Identified peaks are indicated by solid arrows with each frequency. FFT spectra at 2.9, 3.2, 3.4, 3.7 GPa are multiplied by 5 to make uniform the height of the peaks.

We estimate $\frac{1}{F_0}\frac{dF}{dP}$ for each branch by linear curve fitting in the pressure range of $0 < P < P_{CDW2}$, which is listed in Table III. For all branches, $\frac{1}{F_0}\frac{dF}{dP}$ is significantly larger than that expected from the lattice compression, indicating that the change in the cross sections under pressure is dominated by modification of the band structure that is not scaled by lattice deformation. For comparison, the pressure dependence of F for each branch expected from the lattice deformation is shown by the approximately horizontal broken line in Fig. 9(a). This suggests that the deformation effect of the Fermi surface cannot be ignored to discuss the electronic structure under pressure. For the β branch, a previous study has estimated the pressure derivative 0.16 GPa^{-1} [9]. The disagreement with the present study may come from limited data points and pressure region in the previous study. We also estimated the cyclotron effective mass (m_c) from the temperature dependence of SdH oscillations for primary branches, the result of which is summarized in Fig. 9(b). m_c of the β
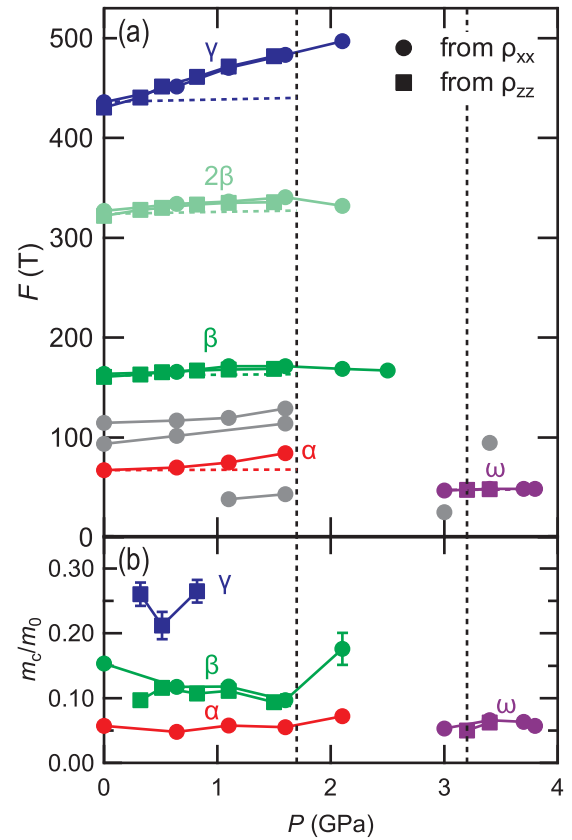

FIG. 9. (a) Pressure dependence of the frequency of SdH oscillation (F) for α, β, γ, and ω branches. Approximately horizontal broken lines indicate the pressure dependence of F expected from the compression of in-plane lattice constant. (b) Pressure dependence of the cyclotron effective mass (m_c) for α, β, γ, and ω branches. The circular and rectangular markers indicate the data obtained from ρ_{xx} and ρ_{zz} measurements, respectively.

and γ branches at ambient pressure were confirmed to be consistent with previous quantum oscillation measurements, as described in Table III. m_c is not so sensitive to the pressure for all branches below P_{CDW2}, and the ω branch in the normal metallic phase above P_{CDW1} holds small effective mass of $\sim 0.066 m_0$. As we can see in Fig. 9, the SdH oscillations observed in ρ_{xx} and ρ_{zz} show quite good agreement with each other. Although all Fermi surfaces should contribute to the transport properties above P_{CDW1}, we found only ω peaks in the B and T range of the present study, possibly due to larger external cross section and heavier cyclotron effective masses of the other orbits compared to ω.

We further focus on the ω branch in the normal metallic phase under pressure. The corresponding cross section in the $\mathbf{k}$ space (S_ω) is estimated to be $S_\omega = 2\pi e F_\omega/\hbar = 4.58\times10^{17}\,\text{m}^{-2}$ with using $F_\omega = 48$ T at 3.4 GPa. Comparing with the cross section of the first Brillouin zone at 3.4 GPa, $S_{BZ} = 2.09\times10^{20}\,\text{m}^{-2}$, S_ω is only 0.22% of S_{BZ}, indicating a quite small cyclotron orbit. Based on the Fermi surface at ambient pressure [9,10], the small ellipsoidal electron pocket located at the X point might be the origin of this frequency. However, whether the Fermi surface at ambient pressure is directly applicable to the case under pressure is unclear at
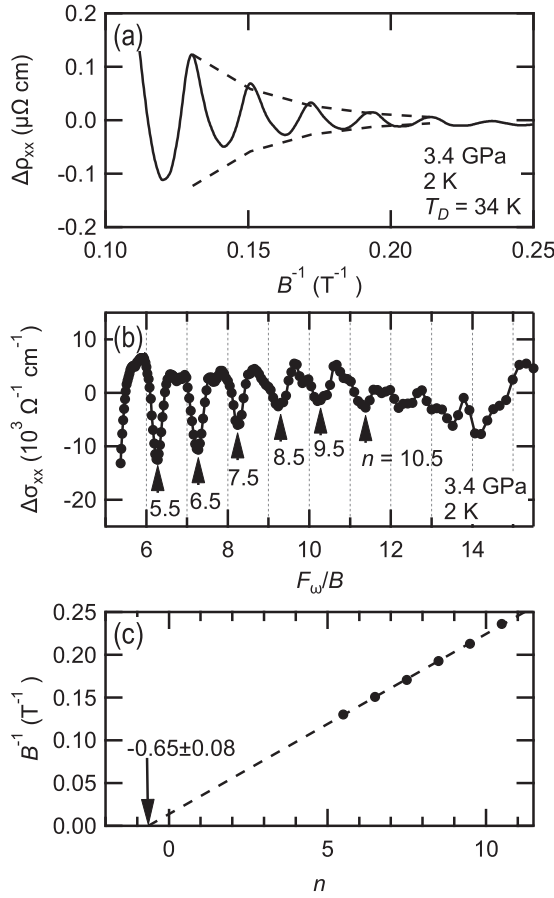
FIG. 10. (a) Oscillatory component of in-plane magnetoresistivity ($\Delta\rho_{xx}$) at $P = 3.4$ GPa and $T = 2$ K as a function of B^{-1}. The dotted curve represents the envelope function reproduced by Dingle temperature of $T_D = 34$ K (see main text). (b) Oscillatory component of in-plane conductivity ($\Delta\sigma_{xx}$) at $P = 3.4$ GPa and $T = 2$ K as a function of F_ω/B. $F_\omega = 48$ T represents the FFT frequency obtained at 3.4 GPa. Fourth-polynomial background was subtracted from the original $\Delta\sigma_{xx}$. Dip positions used to construct (c) are indicated by solid arrows. (c) Inverse magnetic field of the dip positions as a function of Landau index n. The dip positions were assigned to the half-integer n.

present, considering the unignorable band deformation suggested in the pressure dependence of the SdH frequency. Further investigation of the field-angular dependence of this frequency and careful comparison with band calculation under pressure are needed to clarify the geometry of the Fermi surface in the normal metallic phase.

Figure 10(a) shows $\Delta\rho_{xx}$ at $P = 3.4$ GPa and $T = 2$ K as a function of B^{-1}. The SdH oscillation originating from F_ω shows a clear bell-bottom-shaped envelope, which enables the Dingle temperature T_D to be deduced. According to the LK formula, the field dependence of the amplitude $A(B)$ is expected as follows, with cyclotron frequency $\omega_c = eB/m_c$ [31]:

$$A(B) \propto B^{-1/2} \frac{\exp[-2\pi^2 k_B T_D/(\hbar\omega_c)]}{\sinh[2\pi^2 k_B T/(\hbar\omega_c)]}. \qquad (2)$$

From the plot of $\ln\{A(B)B^{1/2}\sinh[2\pi^2 k_B T/(\hbar\omega_c)]\}$ as a function of B^{-1}, $T_D = 34 \pm 2$ K was extracted. Here, we adopted

$m_c = 0.066m_0$, estimated from the temperature dependence of the amplitude at 3.4 GPa. As shown by the dotted curves in Fig. 10(a), the envelope function was reproduced well by Eq. (2), assuming the obtained T_D. Correspondingly, the relaxation time $\tau_D = \hbar/(2\pi k_B T_D)$ and mobility $\mu_D = e\tau_D/m_c$ were estimated as $\tau_D = (3.6 \pm 0.2) \times 10^{-14}$ s and $\mu = 950 \pm 60$ cm^2/(V s), respectively.

To obtain the insight on possible existence of nontrivial band topology in the normal metallic phase above P_{CDW1}, we analyzed the phase factor of the SdH oscillation in the in-plane conductivity σ_{xx}. Figure 10(b) shows the oscillatory component of the in-plane conductivity ($\Delta\sigma_{xx}$) at $P = 3.4$ GPa and $T = 2$ K as a function of F_ω/B. Here, $\Delta\sigma_{xx}$ was obtained by subtraction of the fourth-polynomial background from σ_{xx}. The dips in $\Delta\sigma_{xx}$ were quite sharp, as indicated by the solid arrows in Fig. 10(b), whereas the peaks of $\Delta\sigma_{xx}$, which are ascribed to level-crossing points, exhibited relatively flat figures. We associated the inverse magnetic field of the dip position with the half-integer Landau index, whose relationship is shown in Fig. 10(c). The horizontal intercept of this Landau-level fan diagram is discussed to identify the anomalous phase shift originating from the presence of the Dirac fermion [32,33]. The functional form of $\Delta\sigma_{xx}$ is simplified as

$$\Delta\sigma_{xx} \propto \cos\left[2\pi\left(\frac{F_\omega}{B} + \gamma \pm \delta\right)\right]. \qquad (3)$$

$\gamma = 1/2 - \Phi_B/(2\pi)$ is believed to reflect the Berry phase Φ_B, which is π for a Dirac system and zero for a trivial system. δ depends on the dimensionality of the system: $\delta = \pm 1/8$ for the three-dimensional case and $\delta = 0$ for the two-dimensional case. The above formulation indicates that in the three-dimensional system, the horizontal intercept of the Landau-level fan diagram takes $-1/2 \pm 1/8$ and $\pm 1/8$ for the trivial and Dirac cases, respectively. In the case of the ω branch, the horizontal intercept is determined to be -0.65 ± 0.08, which seems to be close to the trivial case ($-1/2 - 1/8 \sim -0.625$). However, we note that the phase of quantum oscillation is considerably affected by whether Zeeman splitting exists or not [34]. The effect of Zeeman splitting yields an amplitude factor $R_s = \cos[\pi g^* \mu_B B/(\hbar\omega_c)] = \cos(\pi M_{ZC})$, whose sign changes depending on the effective g factor (g^*) and cyclotron effective mass. The flat peaks in Fig. 10(b) may indicate that this branch possesses finite Zeeman splitting, which is inconspicuous, owing to the limited magnetic field range in the present study. Thus, to properly evaluate the topological aspect from SdH oscillation, the value of the Zeeman-cyclotron ratio M_{ZC}, which is an alternative index to discuss the nontrivial band topology [35,36], should be clarified by further high-field or field-angular dependence measurements. The horizontal intercept of the ω branch determined in the present study suggests $2N - 0.5 < M_{ZC} < 2N + 0.5$, where $N = 0, 1, 2, \ldots$. The specification of M_{ZC} remains for future study.

Finally, we focus on the oscillatory component observed below 4 T [dotted area in Figs. 7(a) and 8(a)] in the pressure range of $P_{CDW2} < P < P_{CDW1}$. Figure 11(a) shows the FFT spectra of $\Delta\rho_{xx}$ between 1 and 4 T at 2 K. A FFT peak of ~ 9.2 T is discernible at 1.6 GPa where CDW2 still exists, and it was suddenly enhanced in $P_{CDW2} < P < P_{CDW1}$. As P increases toward P_{CDW1}, the oscillation becomes considerably
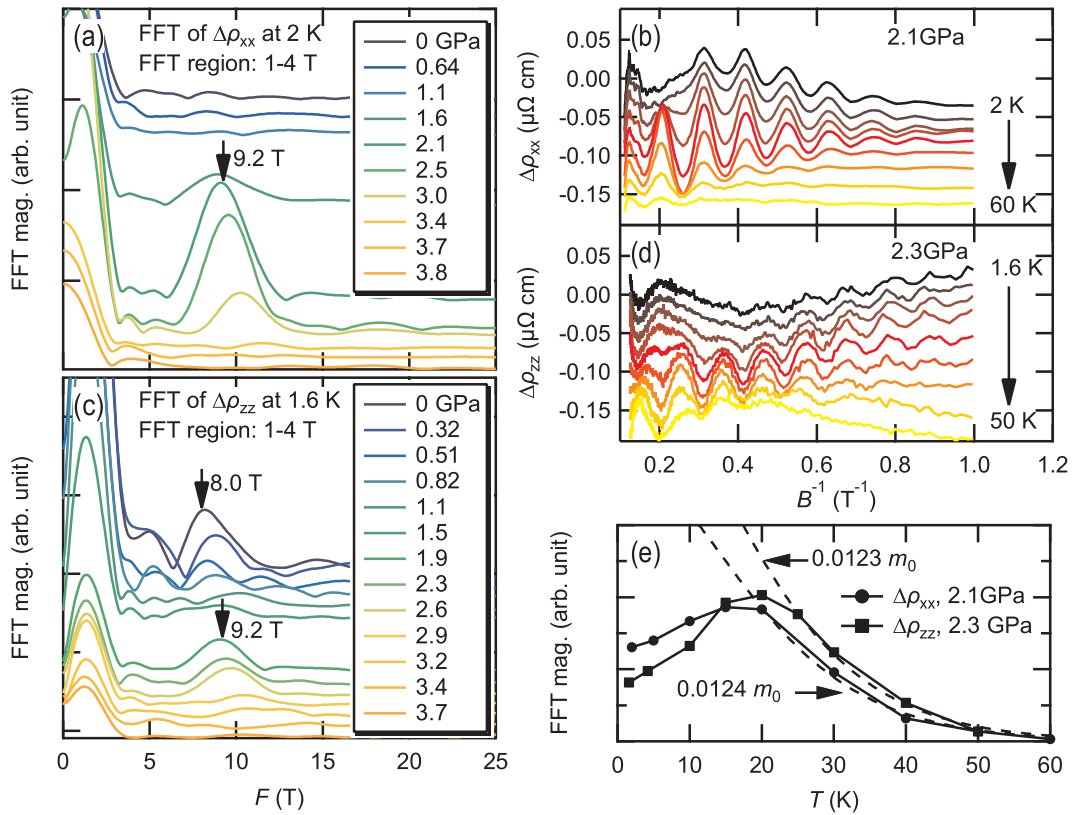
FIG. 11. FFT spectra of oscillatory component of (a) the in-plane magnetoresistivity ($\Delta\rho_{xx}$) at 2 K and (c) out-of-plane magnetoresistivity ($\Delta\rho_{zz}$) at 1.6 K. In (a) and (c), FFT analysis was performed in the magnetic-field region of 1 T $< B <$ 4 T. (b) $\Delta\rho_{xx}$ at 2.1 GPa and (d) $\Delta\rho_{zz}$ at 2.3 GPa as a function of B^{-1}. Each curve is vertically shifted for clarity. (e) Temperature dependence of the FFT magnitude for $\Delta\rho_{xx}$ at 2.1 GPa and $\Delta\rho_{zz}$ at 2.3 GPa. FFT analysis was performed in the magnetic-field region of 1 T $< B <$ 4 T.

damped and is not observed above P_{CDW1}. Figure 11(b) shows the temperature variation of $\Delta\rho_{xx}$ at 2.1 GPa, where the FFT magnitude at 2 K reaches its maximum. We can see that the peak at $B^{-1} = 0.2$ T^{-1} shows anomalous behavior: although it is absent below 10 K, it becomes large as the temperature increases, and then decreases. It seems that the oscillation amplitude at the high-B and low-T region is strongly suppressed for some reason. The oscillation with frequency of $\sim$9.2 T was also reproduced in the out-of-plane resistivity measurement. Figure 11(c) shows the FFT spectra of $\Delta\rho_{zz}$ between 1 and 4 T at 1.6 K. We can recognize the enhancement of the FFT peak with $F \sim 9.2$ T in $P_{CDW2} < P < P_{CDW1}$, which is consistent with the result shown in Fig. 11(a). We can also identify a peak with $F \sim 8$ T at ambient pressure, which is considered to be a long-period oscillation, as described in Fig. 8(a). Whether the oscillation with $F \sim 8$ T at ambient pressure has an identical origin with that observed in $P_{CDW2} < P < P_{CDW1}$ remains unclear at present, although the frequencies are close with each other. Figure 11(d) shows the temperature variation of $\Delta\rho_{zz}$ at 2.3 GPa. The suppression of oscillation amplitude at the high-B and low-T region is seen more clearly.

The distinct peak in the FFT spectrum indicates that this oscillation is periodic as a function of B^{-1}, suggesting a sort of magnetotransport effect. Besides, the frequency is independent of current direction as long as the magnetic-field direction is identical, which agrees with the general feature of the SdH oscillation. However, the significant reduction of the

amplitude observed at the high-B and low-T region is unusual compared with conventional SdH oscillation. Several mechanisms have been known to cause the resistivity oscillation, whose amplitude shows anomalous temperature dependence although they are quite similar with the SdH oscillation. One is called magneto-phonon resonance [37], whose origin is resonant carrier scattering across the Landau levels caused by optical phonons. However, this phenomenon is mostly observed in low-carrier systems such as semiconductors and usually absent below 50 K, where the population of the optical phonon is quite small. These features do not agree with our results. Another example is called the Stark quantum interference [31,38]. The origin of this resistivity oscillation is a quantum interference of the wave function between two open orbits running parallel in the momentum space. However, the oscillation amplitude is expected to be almost independent of temperature unless the orbits are considerably smeared out. Thus, the strong temperature dependence of the resistivity peak at the high-B region cannot be explained by this mechanism. Thus, we ascribe the SdH oscillation as being the most probable origin of this oscillation phenomenon. The deviation from the conventional LK formula may be caused by a change of m_c and/or g^*, though the precise origin is unclear within the scope of the present study. The small frequency of 9.2 T corresponds to the cross section of 8.78×10^{16} m^{-2} in the $\bm{k}$ space, which is only 0.042% of the cross section of the first Brillouin zone at 2.1 GPa. Because such a small

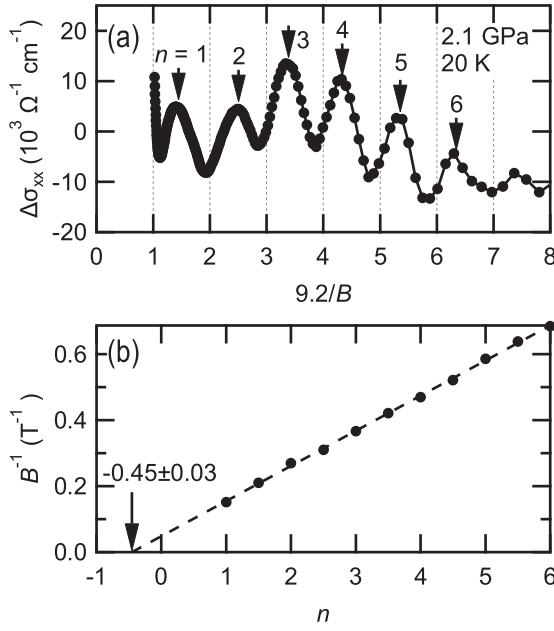FIG. 12. (a) Oscillatory component of in-plane conductivity $\Delta\sigma_{xx}$ at 2.1 GPa and 20 K. Fifth-polynomial background was subtracted from σ_{xx}. Horizontal axis represents the inverse magnetic field normalized by the frequency of 9.2 T. (b) Landau-level fan diagram constructed from the data in (a). The integer n corresponds to the peak in $\Delta\sigma_{xx}$.

cross section is not expected in the band calculation at ambient pressure, the emergence of a small Fermi surface under pressure (Lifshitz transition) or reconstruction of the Fermi surface by nesting of CDW1 is considered to be the possible origin.

Figure 11(e) summarizes the temperature dependence of the FFT magnitude calculated from the data shown in Figs. 11(b) and 11(d). The temperature dependence of the oscillation showed almost identical property between $\Delta\rho_{xx}$ and $\Delta\rho_{zz}$. As shown in the broken lines in Fig. 11(e), the temperature dependence of the FFT magnitude above 20 K is reproduced well by the conventional LK formula with fixed $m_c \sim 0.012 m_0$. The reduction of the FFT magnitude below 20 K reflects the damping behavior described in Figs. 11(b) and 11(b).

Finally, we focus on the phase factor of this small cyclotron orbit. Figure 12(a) shows the oscillatory component of conductivity ($\Delta\sigma_{xx}$) at 2.1 GPa and 20 K. As well as the case of the ω branch, we assigned the peak position to the integer Landau index, and constructed the Landau-level fan diagram shown in Fig. 12(b). The horizontal intercept was estimated to be -0.45 ± 0.03, which seems to be close to the trivial case ($-1/2 + 1/8 \sim -0.375$), or $2N - 0.5 < M_{ZC} < 2N + 0.5$ where $N = 0, 1, 2, \ldots$ using the Zeeman-cyclotron ratio.

IV. CONCLUSION

In conclusion, we comprehensively investigated the magnetotransport properties of LaAgSb$_2$ under high pressure to clarify the phase diagram of the two charge density wave (CDW) states and the change in the electronic structure
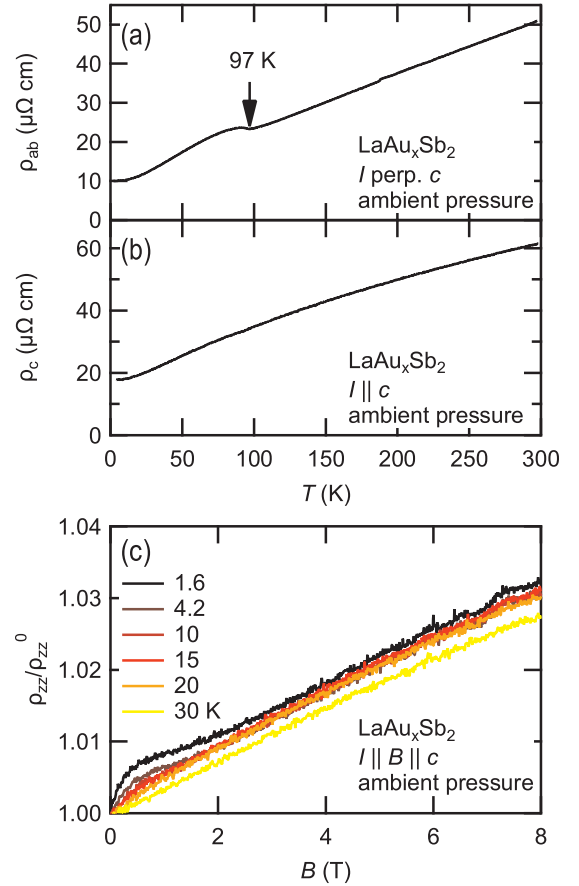

FIG. 13. Temperature dependence of the (a) in-plane resistivity and (b) out-of-plane resistivity in LaAu$_x$Sb$_2$. (c) Out-of-plane magnetoresistivity ($I \parallel B \parallel c$) normalized by zero-field value at ambient pressure.

across the CDW critical pressures. The temperature dependence of in-plane, out-of-plane, and Hall resistivity showed anomalies at $T_{CDW1} \sim 210$ K and $T_{CDW2} \sim 190$ K at ambient pressure; this result agrees with the previous studies. Both T_{CDW1} and T_{CDW2} were suppressed under pressure with rates of -51 and -80 K/GPa, respectively. Compared with LaAuSb$_2$, which shows similar successive CDW transitions, the CDW states in LaAgSb$_2$ seem robust against pressure. The critical pressures of CDW1 and CDW2 were determined to be $P_{CDW1} \sim 3.0$–3.4 GPa and $P_{CDW2} \sim 1.5$–1.9 GPa, respectively.

The ρ_{xx} measurements ($B \parallel c$, $I \perp B$) under pressure showed the quasilinear magnetoresistance effect (1000% in $P < P_{CDW2}$ and $P > P_{CDW1}$, and 4000% in $P_{CDW2} < P < P_{CDW1}$ at 9 T). In-plane Hall conductivity showed a steplike increase at P_{CDW1}. This is qualitatively consistent with the emergence of a two-dimensional hollow Fermi surface, which is regarded to be responsible for the nesting of CDW1. ρ_{zz} ($B \parallel I \parallel c$) showed a prominent negative magnetoresistance effect, which was observed to some extent in all measured pressures from ambient to 4 GPa. The presence of a hollow Fermi surface seems to be insensitive to the emergence of this negative magnetoresistance effect. Additional information

about the Fermi surface under pressure is necessary to understand the field dependence of ρ_{zz}.

We observed clear Shubnikov–de Haas (SdH) oscillation in both ρ_{xx} and ρ_{zz}, whose oscillation frequencies were consistent with those found in the previous quantum oscillation studies at ambient pressure. The pressure dependence of the oscillation frequencies was significantly larger than that expected from the decrease in the in-plane lattice constant, which indicates unignorable deformation of the Fermi surface under pressure. In the normal metallic state above $P > P_{CDW1}$, we observed a single SdH oscillation with a frequency and cyclotron mass of 48 T and $0.066m_0$, respectively. This cyclotron orbit corresponds to only 0.22% of the first-Brillouin-zone area projected on $k_z = 0$. The Landau-level fan diagram analysis suggested the trivial phase factor for this oscillation. In the pressure region in the present study ($P < 4$ GPa), the cyclotron effective mass for each oscillation component showed little pressure dependence. We also identified another oscillatory component below 4 T, which is significantly enhanced for $P_{CDW2} < P < P_{CDW1}$. The oscillation was periodic in terms of the inverse magnetic field and showed an identical frequency of 9.2 T in ρ_{xx} and ρ_{zz}. We ascribe this to an SdH oscillation from its small cyclotron orbit (0.042% of the first Brillouin zone). The amplitude of this SdH oscillation was anomalously suppressed in the low-temperature and high-field region, and its origin has been left for future study.

APPENDIX: ELECTRICAL TRANSPORT PROPERTIES OF LaAu$_x$Sb$_2$

Single crystals of LaAu$_x$Sb$_2$ were obtained by the Sb self-flux method [17]. La (99.9%), Au (99.9%), and Sb (99.9999%) with a molar ratio of 1:2:20 were placed in an alumina crucible, and synthesized by the same process described in LaAgSb$_2$. The temperature dependence of in-plane resistivity (ρ_{ab}) at ambient pressure is shown in Fig. 13(a). We observed a humplike anomaly at $T_{CDW1} = 97$ K, which is ascribed to the CDW transition with higher transition temperature. Based on Ref. [19], the amount x is affected by the initial molar ratio of the elements. Although we did not evaluate the precise amount of Au, T_{CDW1} of our sample seems to be close to the case of LaAu$_{0.947}$Sb$_2$ in Ref. [19]. We could not identify the secondary CDW transition with lower transition temperature, possibly owing to the off-stoichiometric nature. Figure 13(b) shows the out-of-plane resistivity (ρ_c) at ambient pressure. The anomaly at T_{CDW1} is quite weak compared to ρ_{ab}, which is consistent with the previous report [19]. Figure 13(c) shows the longitudinal magnetoresistivity normalized by zero-field value (ρ_{zz}/ρ_{zz}^0) at ambient pressure. The magnetoresistance effect is positive and quite small, which contrasts with the prominent negative magnetoresistance effect observed in LaAgSb$_2$. We note that the sample size and geometry of electrical contact are almost identical to those in LaAgSb$_2$.

[1] G. Grüner, *Density Waves in Solids* (Perseus Publishing, Cambridge, 1994).

[2] M. D. Johannes and I. I. Mazin, Phys. Rev. B **77**, 165135 (2008).

[3] H.-M. Eiter, M. Lavagnini, R. Hackl, E. A. Nowadnick, A. F. Kemper, T. P. Devereaux, J.-H. Chu, J. G. Analytis, I. R. Fisher, and L. Degiorgi, Proc. Natl. Acad. Sci. USA **110**, 64 (2013).

[4] M. Brylak, M. H. Möller, and W. Jeitschko, J. Solid State Chem. **115**, 305 (1995).

[5] D. Johrendt, J. Mater. Chem. **21**, 13726 (2011).

[6] C. Song, J. Park, J. Koo, K.-B. Lee, J. Y. Rhee, S. L. Bud'ko, P. C. Canfield, B. N. Harmon, and A. I. Goldman, Phys. Rev. B **68**, 035113 (2003).

[7] K. D. Myers, S. L. Bud'ko, I. R. Fisher, Z. Islam, H. Kleinke, A. H. Lacerda, and P. C. Canfield, J. Magn. Magn. Mater. **205**, 27 (1999).

[8] Y. Watanabe, Y. Inada, H. Hidaka, H. Kotegawa, T. Kobayashi, T. Matsuda, and D. Aoki, Phys. B: Condens. Matter **378–380**, 827 (2006).

[9] K. D. Myers, S. L. Bud'ko, V. P. Antropov, B. N. Harmon, P. C. Canfield, and A. H. Lacerda, Phys. Rev. B **60**, 13371 (1999).

[10] Y. Inada, A. Thamizhavel, H. Yamagami, T. Takeuchi, Y. Sawai, S. Ikeda, H. Shishido, T. Okubo, M. Yamada, K. Sugiyama, N. Nakamura, T. Yamamoto, K. Kindo, T. Ebihara, A. Galatanu, E. Yamamoto, R. Settai, and Y. Onuki, Philos. Mag. **82**, 1867 (2002).

[11] S. L. Bud'ko, S. A. Law, P. C. Canfield, G. D. Samolyuk, M. S. Torikachvili, and G. M. Schmiedeshoff, J. Phys.: Condens. Matter **20**, 115210 (2008).

[12] T. Arakane, T. Sato, S. Souma, T. Takahashi, Y. Watanabe, and Y. Inada, J. Magn. Magn. Mater. **310**, 396 (2007).

[13] X. Shi, P. Richard, K. Wang, M. Liu, C. E. Matt, N. Xu, R. S. Dhaka, Z. Ristic, T. Qian, Y.-F. Yang, C. Petrovic, M. Shi, and H. Ding, Phys. Rev. B **93**, 081105(R) (2016).

[14] K. Wang and C. Petrovic, Phys. Rev. B **86**, 155213 (2012).

[15] J. R. Chamorro, A. Topp, Y. Fang, M. J. Winiarski, C. R. Ast, M. Krivenkov, A. Varykhalov, B. J. Ramshaw, L. M. Schoop, and T. M. McQueen, APL Mater. **7**, 121108 (2019).

[16] S. Seo, V. A. Sidorov, H. Lee, D. Jang, Z. Fisk, J. D. Thompson, and T. Park, Phys. Rev. B **85**, 205145 (2012).

[17] C. N. Kuo, D. Shen, B. S. Li, N. N. Quyen, W. Y. Tzeng, C. W. Luo, L. M. Wang, Y. K. Kuo, and C. S. Lue, Phys. Rev. B **99**, 235121 (2019).

[18] I. Hase and T. Yanagisawa, Phys. Proc. **58**, 42 (2014).

[19] L. Xiang, D. H. Ryan, W. E. Straszheim, P. C. Canfield, and S. L. Bud'ko, Phys. Rev. B **102**, 125110 (2020).

[20] S. L. Bud'ko, T. A. Wiener, R. A. Ribeiro, P. C. Canfield, Y. Lee, T. Vogt, and A. H. Lacerda, Phys. Rev. B **73**, 184111 (2006).

[21] M. S. Torikachvili, S. L. Bud'ko, S. A. Law, M. E. Tillman, E. D. Mun, and P. C. Canfield, Phys. Rev. B **76**, 235110 (2007).

[22] S. Masubuchi, Y. Ishii, K. Ooiwa, T. Fukuhara, F. Shimizu, and H. Sato, JPS Conf. Proc. **3**, 011053 (2014).

[23] T. C. Kobayashi, H. Hidaka, and H. Kotegawa, Rev. Sci. Instrum. **78**, 023909 (2007).

[24] K. Murata, K. Yokogawa, H. Yoshino, S. Klotz, P. Munsch, A. Irizawa, M. Nishiyama, K. Iizuka, T. Nanba, T. Okada, Y. Shiraga, and S. Aoyama, Rev. Sci. Instrum. **79**, 085101 (2008).

[25] A. A. Abrikosov, *Fundamentals of the Theory of Metals* (North-Holland, Amsterdam, 1988).

[26] F. Arnold, C. Shekhar, S.-C. Wu, Y. Sun, R. D. dos Reis, N. Kumar, M. Naumann, M. O. Ajeesh, M. Schmidt, A. G. Grushin, J. H. Bardarson, M. Baenitz, D. Sokolov, H. Borrmann, M. Nicklas, C. Felser, E. Hassinger, and B. Yan, Nat. Commun. **7**, 11615 (2016).

[27] R. D. dos Reis, M. O. Ajeesh, N. Kumar, F. Arnold, C. Shekhar, M. Naumann, M. Schmidt, M. Nicklas, and E. Hassinger, New J. Phys. **18**, 085006 (2016).

[28] D. T. Son and B. Z. Spivak, Phys. Rev. B **88**, 104412 (2013).

[29] J. Xiong, S. K. Kushwaha, T. Liang, J. W. Krizan, M. Hirschberger, W. Wang, R. J. Cava, and N. P. Ong, Science **350**, 413 (2015).

[30] Y. Awashima and Y. Fuseya, J. Phys.: Condens. Matter **31**, 29LT01 (2019).

[31] D. Shoenberg, *Magnetic Oscillations in Metals* (Cambridge University Press, Cambridge, 1984).

[32] Y. Ando, J. Phys. Soc. Jpn. **82**, 102001 (2013).

[33] H. Murakawa, M. S. Bahramy, M. Tokunaga, Y. Kohama, C. Bell, Y. Kaneko, N. Nagaosa, H. Y. Hwang, and Y. Tokura, Science **342**, 1490 (2013).

[34] K. Akiba, A. Miyake, H. Sakai, K. Katayama, H. Murakawa, N. Hanasaki, S. Takaoka, Y. Nakanishi, M. Yoshizawa, and M. Tokunaga, Phys. Rev. B **98**, 115144 (2018).

[35] Y. Fuseya, Z. Zhu, B. Fauqué, W. Kang, B. Lenoir, and K. Behnia, Phys. Rev. Lett. **115**, 216401 (2015).

[36] H. Hayasaka and Y. Fuseya, J. Phys.: Condens. Matter **28**, 31LT01 (2016).

[37] R. J. Nicholas, Prog. Quantum Electron. **10**, 1 (1985).

[38] R. W. Stark and C. B. Friedberg, Phys. Rev. Lett. **26**, 556 (1971).